

Characterization of Multianode Photomultiplier Tubes for use in CLAS12 RICH Detector

P. Degtiarenko^a, A. Kim^{b,*}, V. Kubarovskiy^a, B. Raydo^a, A. Smith^c

^a*Jefferson Lab, Newport News, Virginia, USA*

^b*University of Connecticut, Storrs, CT 0626, USA*

^c*Duke University, Durham, NC 2770, USA*

Abstract

Characterization of Multianode Photomultiplier Tubes for use in CLAS12 RICH Detector.

Keywords: Ring Imaging Cherenkov detector, Hamamatsu Multianode Photo Multiplier tubes H8500 and H12700, Photon detector, Photomultiplier, Photoelectron, Signal amplitude spectra, Photon detection efficiency

For draft only, to be removed in final version

Contents

1	Introduction	1
2	Laser stand for the MAPMT characterization	2
3	Front-end electronics	3
4	Maroc chip calibration	4
5	Cross talk measurements	5
6	Calibration of laser photon flux	7
7	Mathematical model for the description of the PMT's response	8
8	Characterization of MAPMTs	8
9	Results	10
10	Conclusion	10

1. Introduction

As part of the ongoing study of the structure of nucleons [1] in Hall B at the Thomas Jefferson National Accelerator Facility (JLab) the CEBAF Large Acceptance Spectrometer (CLAS12) [2] aims to accurately identify the secondary particles of high energy reactions, assist in probing the strangeness frontier, and aid in characterizing transverse momentum distribution (TMD) and generalized parton distribution (GPD) functions. Indispensable to this task is the ability to identify kaons, pions, and protons. With the CLAS12 spectrometer providing accurate

momentum measurements the Ring imagine Cherenkov detector (RICH) [3, 4, 5, 6] provides tandem Cherenkov light-cone radius measurements which yield the velocities of near light-speed particles, thus facilitating mass-dependent particle identification.

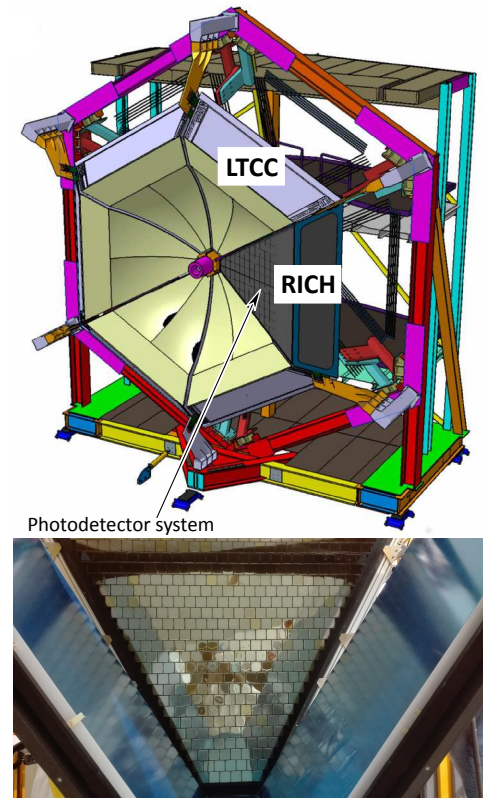


Figure 1: Top: CLAS12 detector with RICH detector covering one out of six sectors. Bottom: the photo-matrix of multianode photomultipliers and mirror system.

The photon detector wall ($\sim 1m^2$) is a crucial component of the RICH detector (see Fig. 1). It is relatively large and should be comprised of many photon detection devices such

*Corresponding author Tel: +1 757 269 6356

Email address: kenjo@jlab.org (A. Kim)

as photomultiplier tubes. Due to the imaging aspect of the RICH they must provide a spatial resolution of less than 1 cm. Since multiple photon detectors are tiled into large arrays, they should have large active area with minimal dead-space. The photon detectors must also efficiently detect single photon level signals and should be sensitive to the visible light due to the aerogel radiator material. Multi Anode PhotoMultiplier Tubes (MAPMTs) are perfect candidates for the CLAS12 RICH detector. They are the flat-panel Hamamatsu MAPMTs offering an adequate compromise between detector performance and cost. Each MAPMT comprises an 8 by 8 array of pixels, each with dimension of 6 by 6 mm. Furthermore, the device has a very high packing fraction of 89% with a high quantum efficiency in the visible light region. The tubes also have excellent immunity to magnetic fields, because all internal parts are housed in a metal package and the distance between dynode electrodes are very short.

Initially, the Hamamatsu H8500 MAPMT model [7] was chosen as the best option because they provide high quantum efficiency for visible light and sufficient spatial resolution ($6 \times 6 \text{ mm}^2$) at a limited cost. However, recently Hamamatsu has released the new H12700 MAPMT model which shows enhanced single photoelectron (SPE) detection and is otherwise similar to the H8500 MAPMTs in spatial resolution and cost. Consequently we desire to better characterize the new H12700 MAPMTs [8] and choose the best model between these two options for inclusion in the CLAS12 RICH.

2. Laser stand for the MAPMT characterization

The large number of the channels in the RICH detector poses challenging problem for the MAPMT testing and calibration. RICH consists of 391 MAPMTs resulting in total number of channels equal to 25024. So in order to test them efficiently within a reasonable timeframe the fully automated test stand was build to evaluate 6 MAPMTs at once, as shown on Fig. 2.

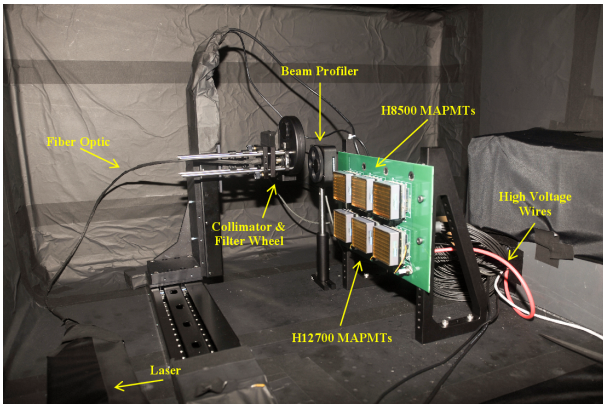
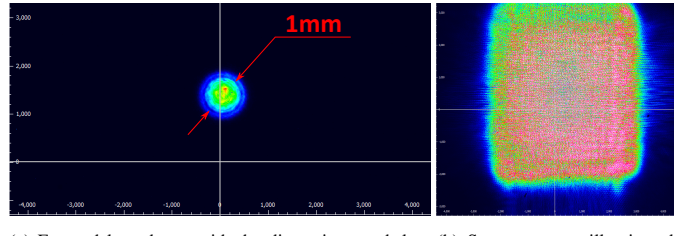


Figure 2: Inner view of the laser stand.

The test stand consists of picosecond diode laser PiL047X with 470 nm wavelength, 2 long travel motorized stands to drive laser fiber in two dimensional space for individual pixel illumination, the motorized wheel with neutral density filter system, 2



(a) Focused laser beam with the dimension much less than the MAPMT pixel size.
(b) Square pattern illuminated all MAPMT surface.

Figure 3: The laser light output options.

adapter boards for MAPMT with JLab designed front-end electronics boards [9]Contalbrigo:2020. The laser light is directed through the fiber and attenuated to the single photon level using the neutral density filters to mimic the conditions of the RICH detector. The motors were remotely controlled to move the focused laser beam across (see Fig. 3a) the entire surface of the MAPMT entrance window and illuminate one by one of all its 64 pixels individually. Another option is to illuminate the whole surface of MAPMT photocathode at once using the Engineered Diffuser to produce square pattern with non-Gaussian intensity distribution (see Fig. 3b).

All laser stand equipment is sitting in the black box with non-reflective black material on the optical table. The laser interlock safety box automatically switch off laser, as well as front-end low voltage electronics and MAPMT high voltage to prevent the possible photomultiplier damage or laser light human illumination in case if somebody will try to open the front door of the black box during the measurements.

This configuration brings routine workload to minimum allowing the evaluation of 6 MAPMTs (equivalent to 328 conventional PMTs!) at 4 different high voltages and 6 different light intensities within 6 hours with less than 15 minutes of human intervention needed to load the MAPMTs to the front-end boards.

Before starting the systematic study of the MAPMT responses, a finer two dimensional scan of several pixels was performed in order to verify the uniformity of the response across pixel's surfaces, as shown on Fig. 4. The horizontal and vertical axes denote laser beam position during the scan. Along the both directions there are obvious drops in efficiency when the laser strikes the space between the pixels. The drops are relatively narrow so the dead-space is very small as expected from the

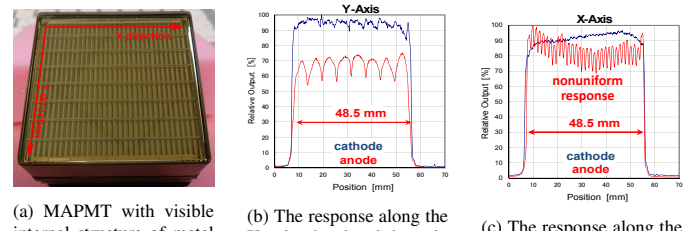


Figure 4: The response uniformity of MAPMT.

Hamamatsu specifications. Additionally, a vertical efficiency variation is visible across the pixel in horizontal scan. These inhomogeneities are correlated with the vertical walls separating dynode chains, owing to the constructional features of the MAPMT. The discontinuity in dynode structure is visible on Fig. 4a. The separate response maps for photocathode shows relatively uniform signal without efficiency drops, confirming that the variation arises from the dynode system.

3. Front-end electronics

The highly integrated front-end electronics with modular design was developed for a large array of MAPMT H12700 to minimize the impact of the electronics material on the detector downstream the RICH. An architecture of the readout electronics consists of front-end cards with dedicated Application Specific Integrated Circuit (ASIC) configured, controlled and readout by programmable devices such as Field Programmable Gate Array (FPGA). The ASIC board is based on the MAROC3 integrated circuit whose excellent single photon capabilities both in analog and binary mode have been confirmed. The final design has consists of stacked PCB layers behind each MAPMT sensor (see Fig. 5). The first layer houses the ASIC front end and ancillary components (e.g. external amplifier) and it is directly connected to the anodes array. A second PCB will host the FPGA in charge of configuring, managing and acquiring one or more ASICs and the low voltage and HV bias distribution. The use of the JLab SSP as controller and collector of the front-end data provides a strong synergy with the current JLab upgrade activity. Data are transmitted on high speed serial (optical) lines minimizing the wiring and therefore the material budget. With that sandwich architecture the total photon detection surface will be covered by a fixed number of basic units or tiles made up by two or three sensor each. The total spacing for electronics will not exceed 20 cm in depth (including MAPMT and mechanical support). The three-tiles electronics module with and without 3 H12700 MAPMTs installed is shown on Fig. 5.

Each MAROC chip consists of 64 independent channels and is equipped with single channel adjustable preamplifier, configurable signal shaping, slow shaper capable of charge measurements and binary output with fast shaping and adjustable threshold. The performance of MAROC chips was tested and was found suitable for RICH requirements:

- 100% efficiency at 1/3 of single photoelectron signal (50 fC)
- time resolution of 1 ns
- short deadtime to sustain the trigger rate of 20 kHz
- latency of 8 μ s

The measurements of custom front-end electronics together with installed MAPMTs in the RICH Black Box setup were crucial for understanding the their performance in the RICH detector in CLAS12. To test and calibrate FE electronics the multiple tests with internal onboard charge injector, external charge injector and signal generator were performed. RICH

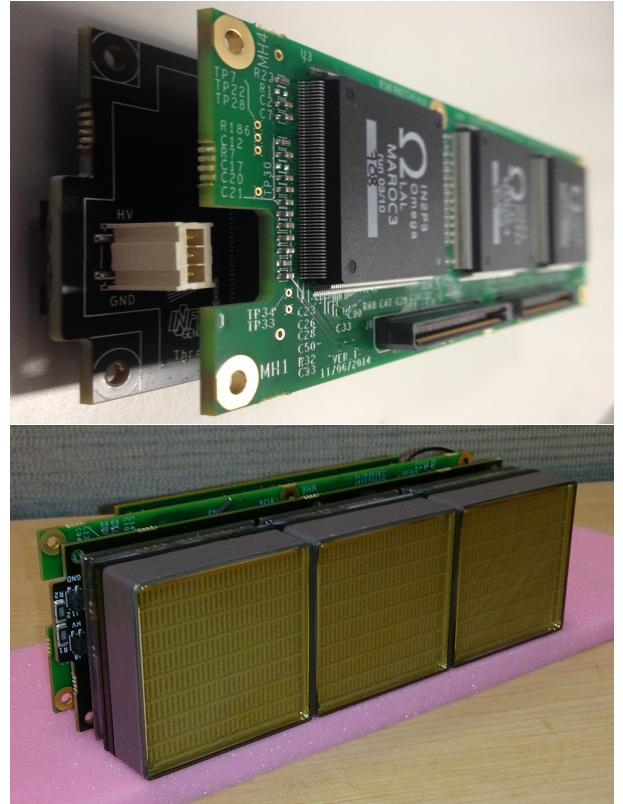


Figure 5: Front-end electronics readout board and mounted MAPMTs.

MAPMT test setup was modified to house two FE boards inside the black box as shown on Fig. 6. The PCB guidelines were installed inside the black box to ensure easy mounting and dismounting procedure universal for both 2-MAPMT and 3-MAPMT FE modules. Each FE module is connected to the low voltage power supply to power FPGA and ASIC boards. The communication between FPGA board and PC is performed using TCP/IP protocol via optical fiber network cable. The HV cables, one per each module, supply power for attached MAPMTs. The Data Acquisition program runs on external PC under Linux OS, configures FPGA and MAROC boards and collects the data through network interface. Similarly to previous configuration, the laser with neutral density filters and light diffuser is installed on a moving platform to allow illumination of individual MAPMTs with different light intensities. The current setup allows fast evaluation of FE modules with highly automatized procedure which is important because RICH panel consists of 113 tiles with 3-MAPMTs and 23 tiles with 2-MAPMTs installed to house 391 MAPMTs.

The MAROC chip used to read MAPMT outputs has two main paths to feed the preamplified input current:

- analog line with a slow shaper which allow the injected charge measurements
- binary line with a fast shaper followed by a discriminator with configurable threshold which allows to deliver trigger outputs

Both lines are independent and highly configurable. The slow

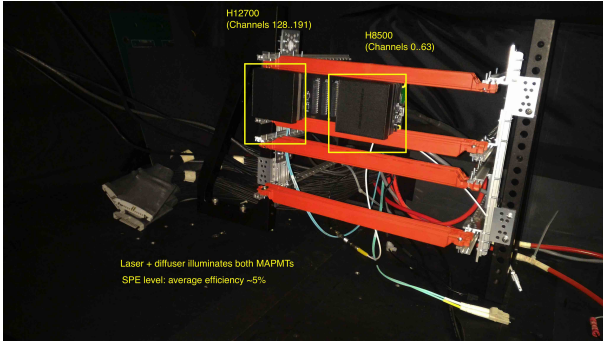


Figure 6: Mount inside RICH Black box is capable to hold two Front-End boards and up to 6 MAPMTs

shaper can not be used during normal operation of RICH detector due to relatively small HOLD latency of 200 ns. It can, however, be used for calibration purposes. On the other hand the digital line with fast shaper is suitable for RICH operation and will be used to detect signals from Cherenkov photons incident on the readout panel.

The preliminary measurements of MAPMTs signal were taken using the FE tile with 3-MAPMTs installed inside the RICH black box. Both lines were evaluated as shown of Fig. 7 and 8. The internal pulse generator was used to trigger laser through its adjustable external trigger input achieving synchronization between light source and MAROC readout. Then the data were collected with both lines collecting data in parallel. Fig. 7a shows the slow shaper waveform for different charge injections from MAROC3 datasheet. On the right Fig. 7b shows the same waveform obtained from the data collected at Jefferson Lab using RICH test setup with laser and MAPMT. In order to reconstruct the waveform of the slow shaper, the hold delays parameters was changed from 1 to 100 and data were collected at different values. This measurements allow us to find the best value of the hold delay for internal ADC conversions which correspond to the signal maximum at around (13 ticks = 104 ns). It ensures the largest precision to the charge measurements. The shape of the analog output waveform is configurable and its gain and peaking speed can be changed.

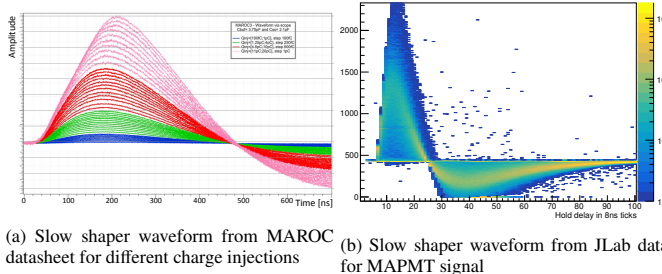


Figure 7: Slow shaper response from MAROC

The digital line can be sampled with a predefined clock on an adequate deep external digital pipeline with event information available promptly in parallel making it suitable for the RICH application. The binary information comes from the discrimination of the fast shaper lines output. On Fig. 8a the

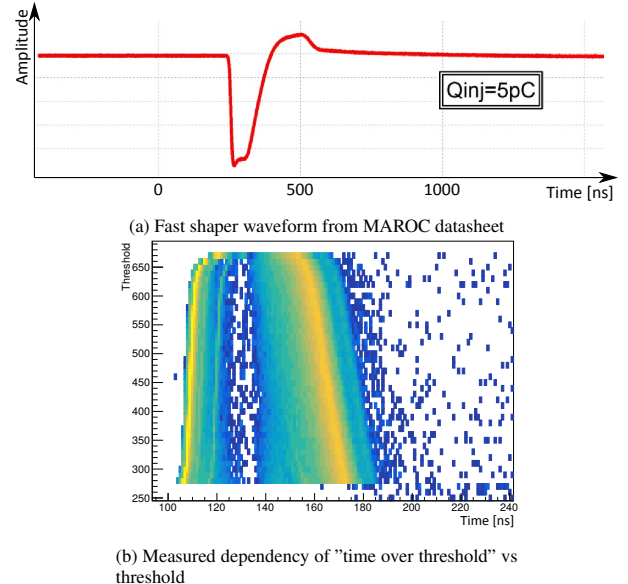


Figure 8: Fast shaper response from MAROC

fast shaper waveform is shown for fixed injected charge from MAROC3 datasheet. On the right fig. 8b shows the dependence of time over threshold versus threshold values. The digital line reports the time when fast shaper waveform crosses the threshold value giving us the leading and trailing edges. To reconstruct fast shaper waveform the measurements with different threshold values were collected and the time of leading and trailing edges were plotted. As expected at higher thresholds the signal crosses the threshold later and has a shorter time over threshold. Also the spread of SPE response from MAPMT gives us preliminary indication of signal's time walk which can be further corrected to improve time resolution. The behaviour at high threshold might not represent the expected performance because the signal reaches saturation and loses its linearity.

Preliminary measurements of MAROC3 and MAPMTs demonstrate good time and charge resolution allowing to further improve our MAPMTs measurements and their understanding. The final production of FE boards is nearly complete and we expect to start receiving FE tiles within the next month.

4. Maroc chip calibration

To remove the non-linearity within the ADC readout, a procedure was developed to convert the amplitude of the MAROC slow shaper signal from ADC channels into charge. The MAROC has a built-in charge injection functionality consisting of a test input pin which is connected to the preamplifiers through a logic network of switches and 2 pF capacitors. Together with an external step function generator, this can be used to inject a controllable amount of charge directly into the preamplifiers. We measured the output of the slow shaper in ADC channels for 82 different input charges ranging from 0 to 4 pC. Fig. 9 shows the relationship between the injected charge and the measured amplitude in units of ADC channels for three different readout channels. The relationship between charge and ADC channels

is linear up to about 1.5 pC. This distribution was observed to vary between chips and pixels, and thus a unique distribution was measured for all 64 pixels on each MAROC used in this study.

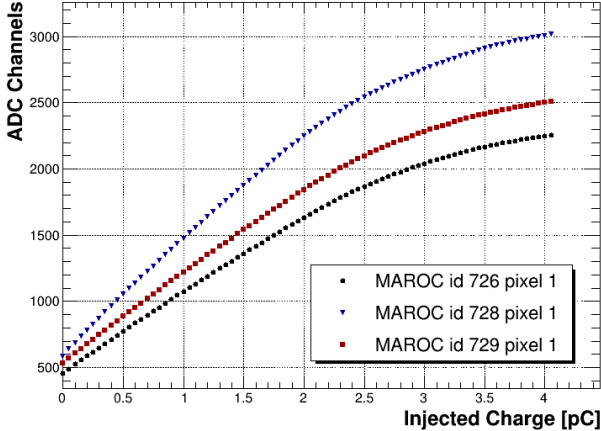


Figure 9: Response of MAROC slow shaper in ADC channels as a function of the injected charge. This curve is for MAROC id 726 and pixel 01.

This calibration data was used to convert the measured amplitude in ADC channels into charge collected on an event-by-event basis. The interpolation is done by assigning quadratic functions to every calibration data point to obtain local estimates of the charge as a function of ADC channels. The quadratic functions are obtained by fitting the nearest 5 data points, so that the value of the function is not constrained to equal the measured ADC channels at the given injected charge. For each event, the charge is estimated as a linearly weighted average between the extrapolations of the quadratic functions from the nearest two data points. Fig. 10 and Fig. 11 show typical amplitude distributions before and after this conversion is applied for one H12700 MAPMT pixel and one H8500 MAPMT pixel, respectively. For both, the conversion to charge extends the high-amplitude tails of the spectra due to the nonlinearity of the ADC readout.

5. Cross talk measurements

To demonstrate the crosstalk between adjacent pixels on the MAPMTs, we collected data where the whole PMT face was masked with a sheet of black paper, and a single 3mm diameter hole was punctured over the center of one pixel. Despite the majority of the laser light being incident on the single unmasked pixel, we observed signals above pedestal in the surrounding pixels as well. Fig. 12 shows the measured spectra for the central and neighboring pixels when the puncture hole was directly above pixel 29. There are two types of events we see in this data set for the pixels surrounding the illuminated pixel. The first is the electronic crosstalk resulting from the electron cascade in the central pixel. The signal measured in a neighboring pixel is directly proportional to that which is measured in the central pixel. In Fig. 12, these types of events are characterized by

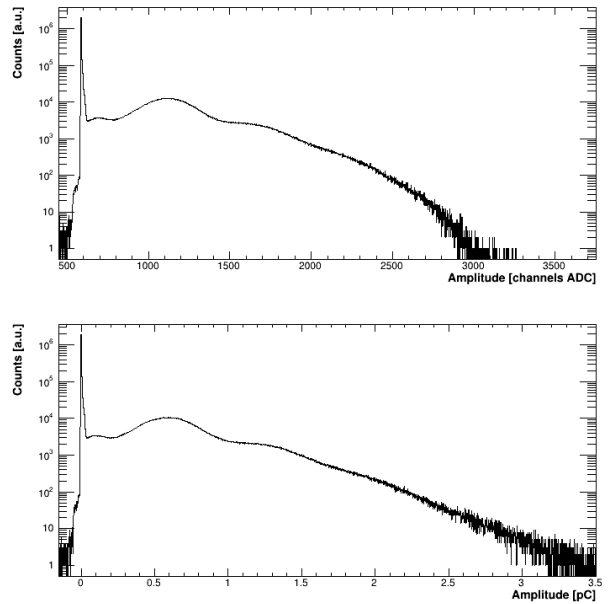


Figure 10: Top: A typical spe spectrum for one HA12700 pixel in units of ADC channels. Bottom: The same spectrum after converting the units into pC.

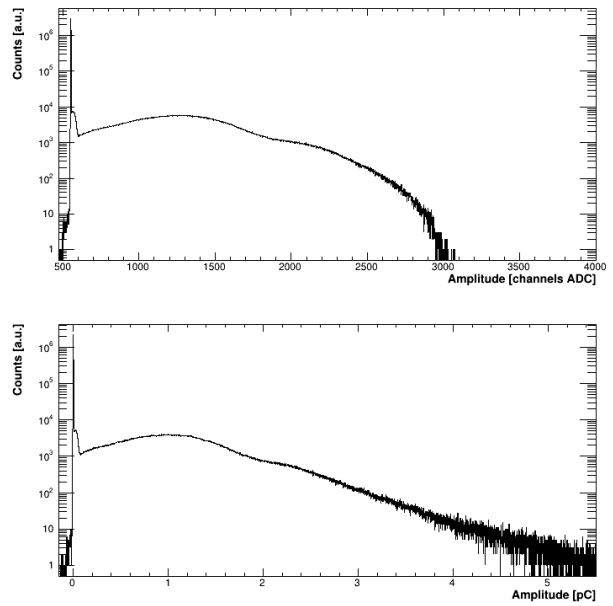


Figure 11: Top: A typical spe spectrum for one HA8500 pixel in units of ADC channels. Bottom: The same spectrum after converting the units into pC.

a shoulder attached to the right of the pedestal. This is most prominently seen in the spectrum for the pixel directly to the right of the central pixel of Fig. 12 (pixel 30). Because of the strong correlation of the crosstalk to the central pixel, these types of events can be identified and removed from the data offline. More will be discussed on this later.

The second type of event observed in the neighboring pixels of this data comes from the displacement of the photoelectron emitted by the photocathode. When the incident photon hits

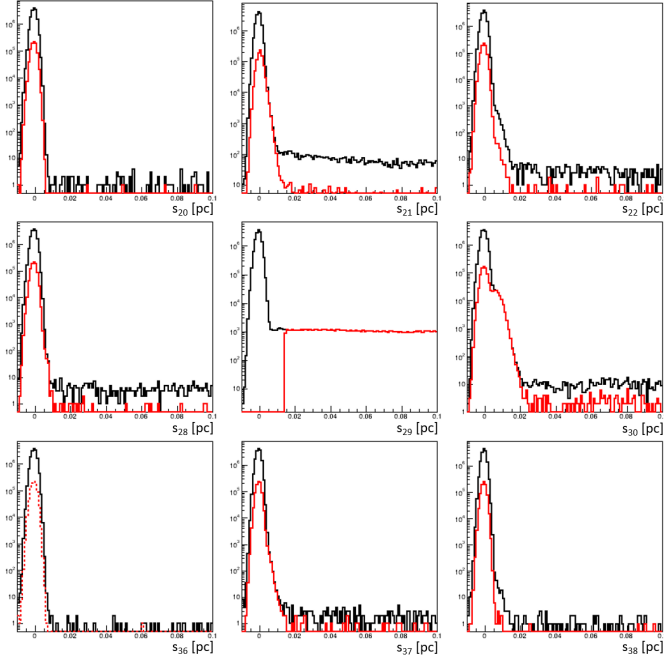


Figure 12: Black: the charge spectra for pixel 29 of a typical H12700 MAPMT and the surrounding pixels when only pixel 29 was illuminated by the laser light. Red: the same spectra with the cut that the signal in pixel 29 is 10σ above pedestal.

pixel 29, there is some probability that the emitted photoelectron is detected by one of the neighboring pixels. Because there is no correlation with the central pixel for these events, there is no way to identify these signals on an event-by-event basis. In Fig. 12, the spectra drawn in red have the additional cut applied that the signal in the central pixel should be greater than 10σ above the pedestal. With this cut applied, the number of events beyond the crosstalk shoulder in the neighboring pixels is reduced by more than an order of magnitude.

Using this masking scheme, we collected data with different pixels unmasked and measured the fraction of events where we observe cross talk in the neighboring pixels. Fig. 13 shows these fractions for four pixels.

To properly characterize the single photoelectron spectrum for each pixel, one needs to either add a description of the crosstalk into the mathematical model for the s.p.e. response, or one can attempt to identify and remove these crosstalk events from the data. A simple procedure was developed and implemented to attempt the latter option. Because the amplitude of the crosstalk is linearly dependent on the amplitude of the photo-induced signal, the crosstalk events appear as linear bands in the plots showing the measured charge in one pixel as a function of the measured charge in a neighboring pixel. Fig. 14 and Fig. 15 show these two dimensional plots for all pixels which neighbor pixel 29 for one H12700 MAPMT and one H8500 MAPMT, respectively. The data shown in these plots were taken with the entire face of the MAPMTs illuminated by the laser light. From these two plots it is obvious that the strength of the crosstalk is vastly different between the H12700 and H8500 MAPMTs. On average, the amplitude of the crosstalk in an

2.2e-01 1.5e-03		1.8e-03 2.0e-04					
6.5e-04 5.7e-05	2.0e-03 1.3e-04	5.7e-04 3.5e-05					
			5.3e-04 1.6e-05	2.9e-02 1.5e-03	7.3e-04 8.2e-05		
			8.6e-04 6.3e-05		1.4e-01 6.7e-04		
			4.2e-04 9.3e-06	2.9e-03 1.1e-04	3.7e-04 2.8e-05		
					5.7e-04 4.5e-05	2.9e-02 8.9e-04	7.4e-04 1.1e-04
	3.1e-03 1.8e-04	5.3e-02 6.5e-04			3.1e-03 2.8e-04		1.0e-01 5.1e-03

Figure 13: For each highlighted pixel a separate run was taken where only this pixel had a 3mm hole punctured in the mask covering the whole PMT face. The numbers in black in the surrounding pixels represent the fraction of events where there is crosstalk in that pixel.

H12700 MAPMT is only about 2-3% of the main signal, whereas the crosstalk amplitude in an H8500 MAPMT can be as large as 50% of the main signal. As we will discuss later, this fact makes it more difficult to address the crosstalk for the H8500 MAPMTs in the mathematical description of the spe response function.

Other noteworthy features from Fig. 14 and Fig. 15 are that the crosstalk signals are strongest in the pixels immediately to the right and left of the pixel where light was incident. The crosstalk bands in those pixels have the largest slope. Most of the crosstalk is contained within the 4 pixels which share an edge with the illuminated pixel, as the plots for the pixels on the corners show little correlation with the charge measured in the central pixel.

Because the crosstalk events are easily distinguished in these two dimensional plots, a cut can be placed to remove these events from the data. The cut is applied to each pixel separately, and is a linear function of the charge measured in that pixel. Specifically, the cut places a limit on the maximum charge measured in the neighboring pixels. If the maximum neighboring charge is above the cut value for the central pixel's measured charge, then the event is tagged as crosstalk and is removed from the charge spectrum for the central pixel. This cut is shown as a dashed (red) line in Fig. 14 and Fig. 15. The start of the cut line is placed 7σ above the pedestal to avoid removing pedestal events. Although the slope of the cut line used here is the same for each pixel on a given PMT.

The main drawback of this crosstalk cut is that it removes events where adjacent pixels both happen to have a photoelectron emitted from the same laser trigger. However, the fraction

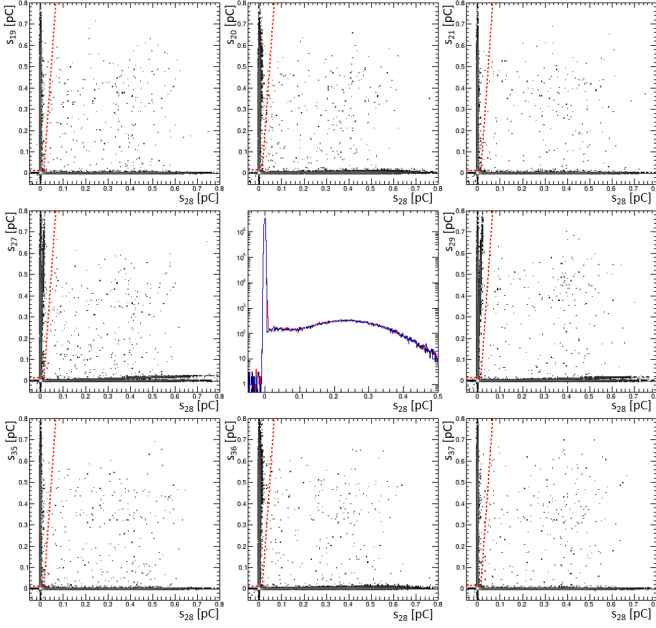


Figure 14: The charge measured in adjacent pixels is plotted as a function of the charge measured in pixel 29 for a typical H12700 MaPMT. The central plot shows the charge spectrum before (red) and after (blue) removal of the crosstalk events which are cut by the dashed (red) line on the 2-dimensional plots.

of these accidental coincidence events is low when the laser filter is used at the minimal setting, meaning at low light intensity this procedure can be used to provide the spe spectrum free from electronic crosstalk. The charge spectra before and after the removal of the crosstalk events in this manner is compared in the central plot in Figs. 14 and 15. For both the H12700 pmt and the H8500 the crosstalk shoulder to the right of the pedestal is removed after applying this cut.

6. Calibration of laser photon flux

The calibration of the absolute laser photon flux was performed with the use of the silicon photodiode Hamamatsu S2281. The tabulated quantum efficiency of this diode at the wave length of our laser ($\lambda = 470$ nm) is 62.6%. The active part of the diode is a circle with a diameter of 11.3 mm, which is 100 mm². The picoammeter KEITHLEY 6485 was used to measure the average diode current while illuminated by the laser beam. The noise diode current was estimated to be at the level of 0.2 pA. During the MAPMT characterization, the laser frequency was maintained at 20 kHz. For light calibration, the higher the frequency, the better current measurement accuracy may be achieved from point of view the noise level. The maximum frequency of our laser is 1 MHz. However, there are additional systematic uncertainties associated with the extrapolation from one frequency to another. For this reason, the scan of the light field was done at a working frequency of 20 kHz. The measured current in the center position of the laser head was around 29.2 pA at this frequency, meaning the systematic uncertainty of this measurement was below 1%. We made a detailed 2D scan of the photon flux by moving the laser head with step sizes of 2

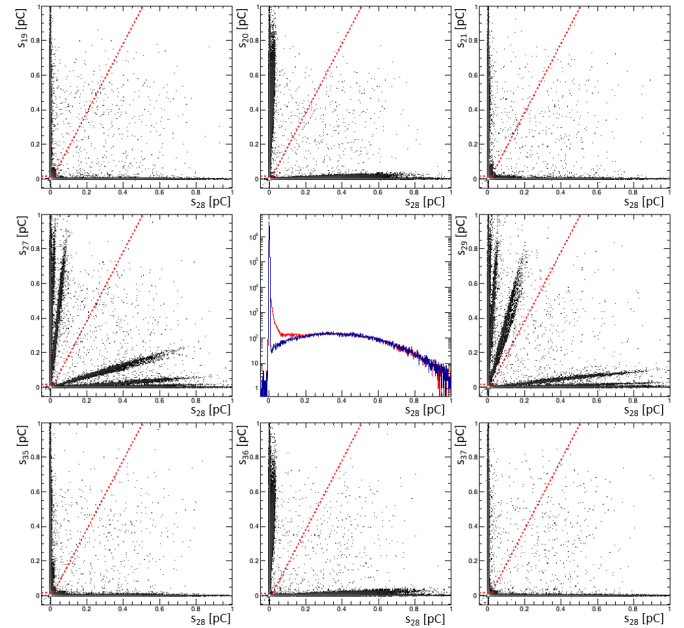


Figure 15: The charge measured in adjacent pixels is plotted as a function of the charge measured in pixel 29 for a typical H8500 MaPMT. The central plot shows the charge spectrum before (red) and after (blue) removal of the crosstalk events which are cut by the dashed (red) line on the 2-dimensional plots.

mm in the X and Y directions along the full area where the 3 MAPMTs were located during the characterization procedure. Normalized to one laser pulse and one mm² area, the number of photons with $\lambda = 470$ nm is presented in Fig. 16. The maximum value of the photon flux in the center of the light field equals 145 $\gamma/\text{mm}^2/\text{pulse}$. These measurements were done without any optical filters installed. We used neutral density calibrated optical filters with antireflection coating. To check the possible filter effects we made a measurement of the light flux for one of the filters with a tabulated attenuation of 100. This test was done with a frequency of 1 MHz to increase the accuracy of the current measurement. The ratio of the measured attenuation factor to the tabulated one was determined to be 1.05 ± 0.01 . This coefficient was applied to the map of the photon flux when used for data with optical filters. It takes into account the possible effects of rescattering or reflection of the photons by filters.

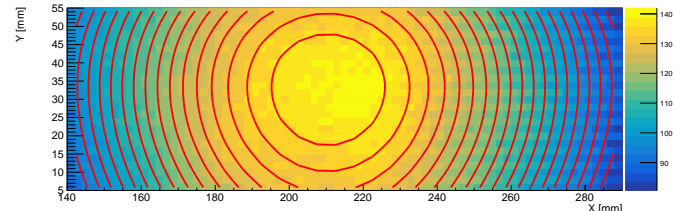


Figure 16: Number of photons per mm² in one laser pulse.

The knowledge of the absolute number of photons hitting the photomultiplier tubes during the characterization gave us the possibility to measure the quantum efficiency of the MAPMTs

for each pixel. The average number of photoelectrons, μ , is proportional to the quantum efficiency:

$$\mu = \epsilon_{Q.E.} \int_{S_{pixel}} \frac{dN_\gamma}{dS} dS$$

where $\int_{S_{pixel}} \frac{dN_\gamma}{dS} dS$ is the number of photons integrated over the pixel's area, S_{pixel} , and $\epsilon_{Q.E.}$ is the quantum efficiency of the pixel. Integration included the measured light field at the position of the pixel under study. The parameter μ was determined during the PMT characterization.

7. Mathematical model for the description of the PMT's response

We started by using a model for signal amplitude distribution based off of Gaussian single photoelectron spectra as discussed in [9] that works reasonably well for H8500, but this model does not satisfactorily treat the spectra seen in the new H12700 MAPMTs from Hamamatsu. Consequently, Pavel Degtarenko [10] has developed a more complicated model using several Poisson components to better fit the MAPMT spectra, especially in the single photoelectron cases. This mathematical model features a realistic description of the MAPMT response where each parameter corresponds to the physical process inside the MAPMT. The SPE spectrum is fitted with a function used to describe the signal amplitude distribution measured by the MAPMT as shown on Fig. 17. The probability of an initial photon to knock out a photoelectron is distributed according to the Poissonian $P(m; \mu) = \frac{\mu^m e^{-\mu}}{m!}$. To approximate the performance of the first amplification cascade of the MAPMT the function $T(n, m; t)$ is introduced in the model as trinomial sum of three Poissonians with different average secondary multiplicities and the corresponding three relative probabilities for every photoelectron to generate secondary electrons. The function $G(a, n; \sigma)$ corresponds to the realistic DAQ measurement function to introduce the experimental resolution into the resulting model function.

The model is found to describe well the amplitude distributions measured at different levels of radiation with different supply voltages. The parameters provide MAPMT characteristics independently of the test measurement conditions (see Fig. 18): the *scale* parameter is virtually independent on the light radiation level while strongly dependnt on high voltage supply, the exact behavior one would expect from the characteristic of internal dynode system of MAPMT.

Currently we have tested 80 H8500 and 260 H12700 (the largest collection of these new MAPMTs in the world). The accumulated data provide an immense knowledge about quantum and collection efficiencies of MAPMTs, their surface uniformity, single photoelectron (SPE) spectrum resolution etc. This parameterized information extracted from the fit of each pixel for every MAPMT is used to describe the detector response in the future simulation.

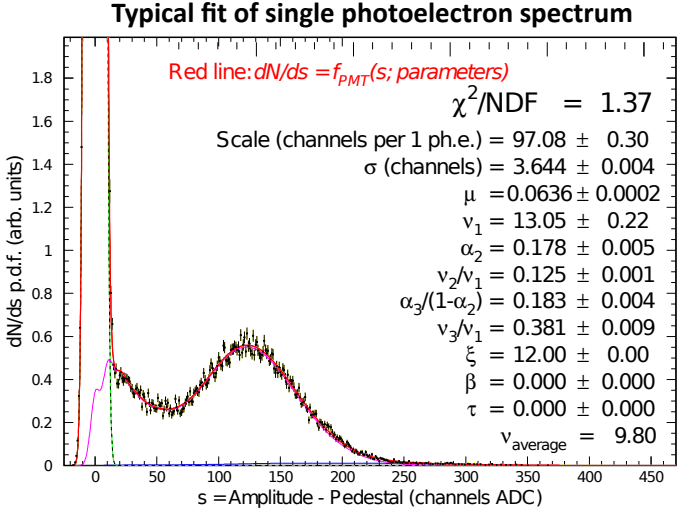


Figure 17: Sample of single photoelectron spectrum from one of the pixels at 1000 V with low intensity laser light source, where integer m corresponds to the number of photoelectrons created at the first stage of the photodetector (photocathode) by the incident light during one event of radiation, index n corresponds to the number of electrons generated at the second stage of the photodetector (first dynode).

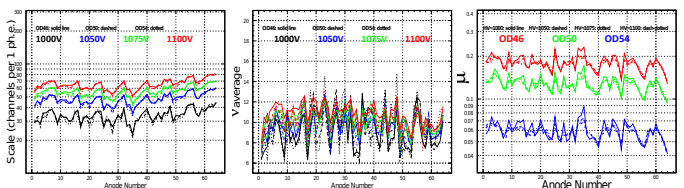


Figure 18: Distributions of fit parameters among the pixels for measurements with 4 different high voltage supplies and 3 different light intensities: the parameter *scale* characterizes the amplification (dynode) system, v - first dynode performance, μ relates to the quantum efficiency (photocathode performance).

8. Characterization of MAPMTs

The performance of MAPMTs was evaluated under certain high voltages. The single photoelectron spectrum and the pixel efficiency for H12700 MA-PMTs were tested and analyzed at 1000v, 1050v, 1075v, and 1100v. The measurements performed at the reference supply voltage of 1000 V were compared to the measurements at different HV values in order to study the behavior of the MAPMT response as a function of the supply voltage. As expected, it was found that the H12700 MA-PMTs perform the best in the single photoelectron spectrum efficiency at higher voltages, especially at 1100v. We see a significantly improved separation of the first photoelectron peak from the pedestal at higher voltage supplies (see Fig. 19). When the average deficiencies of the tested MA-PMTs were analyzed, it was found that the average efficiency for 1000v, 1050v, 1075v and 1100v were approximately 4.6%, 4.9%, 5.0%, and 5.2%, respectively. Therefore, the increase in detection efficiency is found to be over 10% at 1100 V in comparison to 1000 V supply. This separation is the crucial point for a single photon counting detectors such as CLAS12 RICH, where the occupancy is at the level of one photon per pixel.

It was also found that as the gain of the MAPMT increased,

OLD data, to be removed

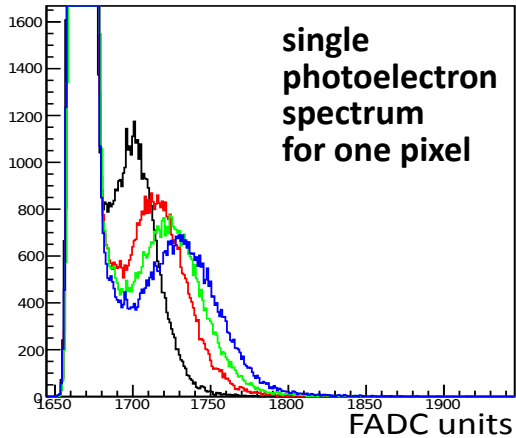


Figure 19: SPE spectra at 1000 (black), 1050 (red), 1075 (green) and 1100 (blue) V.

OLD data, to be removed

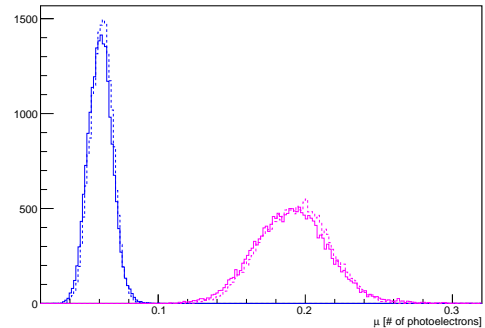


Figure 21: Average number of the photoelectrons emitted from the photocathode for different laser light intensities: $10^{-5.4}$ - blue and $10^{-4.6}$ - red. Solid line is for measurements at 1000 V and dashed - at 1100 V

the efficiency ratio of 1100V to 1000V decreased. The ratio is shown on Fig. 20 as a function of MAPMT gain reported by Hamamatsu. The high voltage supply improves the performance of MAPMT dynode system, decreasing the fraction of the single photoelectron events below the pedestal peak. This indicates that lower gain MAPMTs have a greater difference in the efficiencies at 1100V and 1000V, while higher gain MAPMTs have a smaller difference between the two voltage efficiencies. The improvement for lower gain MAPMTs is more significant than for higher gain MAPMTs, because the high gain MAPMT has good separation of signal from pedestal even at the reference 1000 V. Therefore, the low gain MAPMT benefit greatly from higher supply voltage. The collected data are used to determine what high voltage the MAPMTs should be ran at to acquire the best results when the RICH detector is completed.

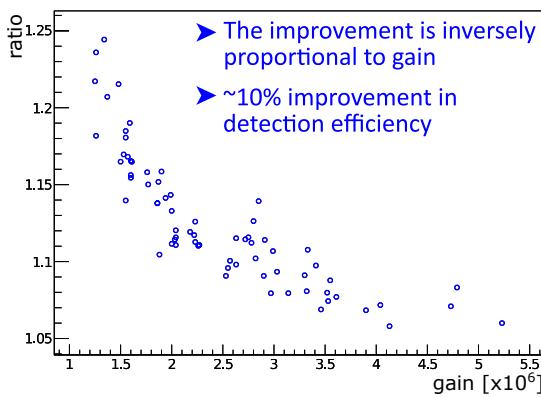


Figure 20: Ratio of MAPMT efficiencies at 1100 and 1000 V as a function of MAPMT gain.

The parameters from Pavel's PMT response function are shown on the Fig. 21 and 22 and correspond to the emission of the photoelectron (μ), its collection and multiplication on the first dynode (*scale* and *v*). We have omitted other parameters that take into account the resolution effects of readout

system or correspond to the cascade multiplication of the secondary electrons as they are out of scope focus of our analysis. Given our requirements for single photoelectron signal sensitivity MAPMTs of our choice should be able to detect with high probability single photon that reaches photocathode. In order to achieve this goal MAPMT should have high quantum efficiency of the photocathode as well as high collection efficiency of produced photoelectron combined with substantial signal multiplication to achieve good resolution of SPE peak. These characteristics were studied in bulk for all 27520 channels (430x64) during the different light conditions and for different supplied HV values.

Fig. 21 shows the distribution of parameter μ which correspond to the average number of the photoelectrons produced during the measurements. This parameters represents the convolution of the MAPMT photocathode quantum efficiency and laser setup light intensity. Both characteristics should not depend on HV supply values and it is demonstrated on this figure by comparison of μ values extracted for the measurements at 1000 V and 1100 V. However one can change the parameter by varying the laser light intensity which is evident from the left shift of μ values for lower light intensity measurements.

The other two free parameters are plotted on Fig. 22. They correspond to the average number of second-stage electrons produced on the first dynode by photoelectron (see Fig. 22a and average signal amplitude for single photoelectron spectrum (see Fig. fig:scale). Both parameters characterize mainly the amplifying subsystem of MAPMT and therefore should depend on supplied HV. The measurements at 1000 V and 1100 V confirm that amplification is improved at higher values of applied high voltage. Traditionally the second parameter (gain) is often used to describe the amplification abilities of photomultipliers and often used in calibration and reconstruction procedures. And it was shown that the extracted gains do not depend on the light conditions with a high degree of accuracy.

9. Results

Large number of MAPMTs from Hamamatsu (XX of H8500 type, and XXX of H12700 type) were studied using the dedicated test stand at JLab. Their performance as single photon detectors was evaluated and characterized in conditions close to their future operations in the CLAS12 RICH detector.

Parameters of the single photoelectron response function of every pixel were extracted using the SPE spectra approximations in our mathematical model, modified to take into account the effects of the signal cross-talk between the neighboring pixels. The stability and consistency of the parameter values measured in different conditions of illumination and at different applied high voltages allows to characterize the intrinsic features of every pixel, independent on the measurement conditions. Absolute quantum efficiency and electronic gain of every channel, as well as the set of parameters describing variable shapes of the SPE functions were measured.

The parameter database accumulated as the result of this work may be used for the selection of the PSPMTs for installation in the RICH detector, and for the optimization of the future run parameters, such as the tube placement selection, setting the values of operating high voltage, electronics gains and thresholds in the detector.

The data also provide the opportunity to evaluate the spread of such parameters in the mass production of the PSPMT devices as the channel gains, quantum efficiencies, SPE spectral shapes, parameters of the cross-talk, - across the face of each tube, and across the whole set. The results show that the quality of PSPMT mass production at Hamamatsu is high and satisfies our needs in the good quality single photoelectron detection.

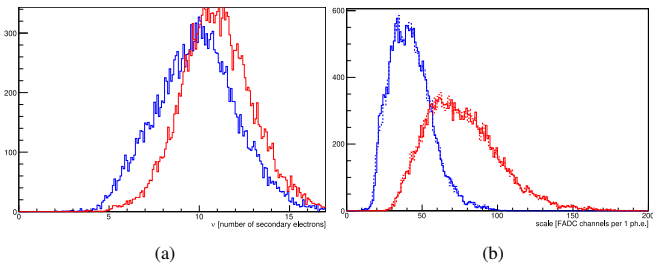


Figure 22: Characteristic parameters of single photoelectron signal distributions from Hamamatsu H12700 MAPMT in the framework of Pavel Degtiarenko's model for measurements at different HV: 1000 V (blue) and 1100 V (red): (a) average number of second-stage electrons knocked out of the first dynode, (b) the average signal amplitude per single photoelectron for different light intensity measurements: at $10^{-5.4}$ (solid line) and at $10^{-4.6}$ (dashed) attenuation

10. Conclusion

We have tested several hundreds of the Hamamatsu H12700 and H8500 multi-anode photomultiplier tubes in order to evaluate the application of these MAPMTs in the Ring Imaging Cherenkov detectors. The PMT's performance study was done using the laser stand with low light illumination to simulate one-photoelectron regime as expected in the real experiment. We were using the state-of-the-art mathematical model for the characterization of the photomultipliers that were design to describe the PMT's signals with low number of photoelectrons. The model was modified to take into account the effects of the cross-talk between the neighboring pixels. The stability and consistency of the parameter values measured in different laser beam intensities and at different applied high voltages allows to characterize the intrinsic features of every pixel, independent on the measurement conditions. We compared the following parameters of two types of MAPMT: H12700 and H8500

- The shapes of the one photoelectron spectra
- PMT's gain as a function of high voltage
- Amplification of the first dynode
- Efficiency to detect one-photoelectron signal
- Detailed comparison of the cross-talk characteristics
- Quantum efficiency of each pixel

The large amount of PMT's gives us the possibility to do statistical analysis of all parameters in hands and compare the performance of H12700 and H8500 for an application in high energy and nuclear physics. The parameter database accumulated as the result of this work may be used for the selection of the PSPMTs for installation in the RICH detector, and for the optimization of the future run parameters, such as the tube placement selection, setting the values of operating high voltage, electronics gains and thresholds in the detector. The data also provide the opportunity to evaluate the spread of such parameters in the mass production of the MAPMT devices as the channel gains, quantum efficiencies, SPE spectral shapes, parameters of the cross-talk, across the face of each tube, and across the whole set. The results show that the quality of MAPMT mass production at Hamamatsu is high and satisfies our needs in the good quality single photoelectron detection.

References

- [1] H. Avakian, et al. (CLAS), Measurement of Single and Double Spin Asymmetries in Deep Inelastic Pion Electroproduction with a Longitudinally Polarized Target, Phys. Rev. Lett. 105 (2010) 262002.
- [2] V. D. Burkert, et al., The CLAS12 Spectrometer at Jefferson Laboratory, Nucl. Instrum. Meth. A959 (2020) 163419.
- [3] M. Contalbrigo, et al., The CLAS12 Ring Imagine Cherenkov Detector, Nucl. Instrum. Meth. A960 (2020) 22–27.
- [4] M. Contalbrigo, et al., Single photon detection with the multi-anode CLAS12 RICH detector, Nucl. Instrum. Meth. A952 (2020) 162123.
- [5] M. Mirazita, et al., The large-area hybrid-optics RICH detector for the CLAS12 spectrometer, Nucl. Instrum. Meth. A876 (2017) 54–58.

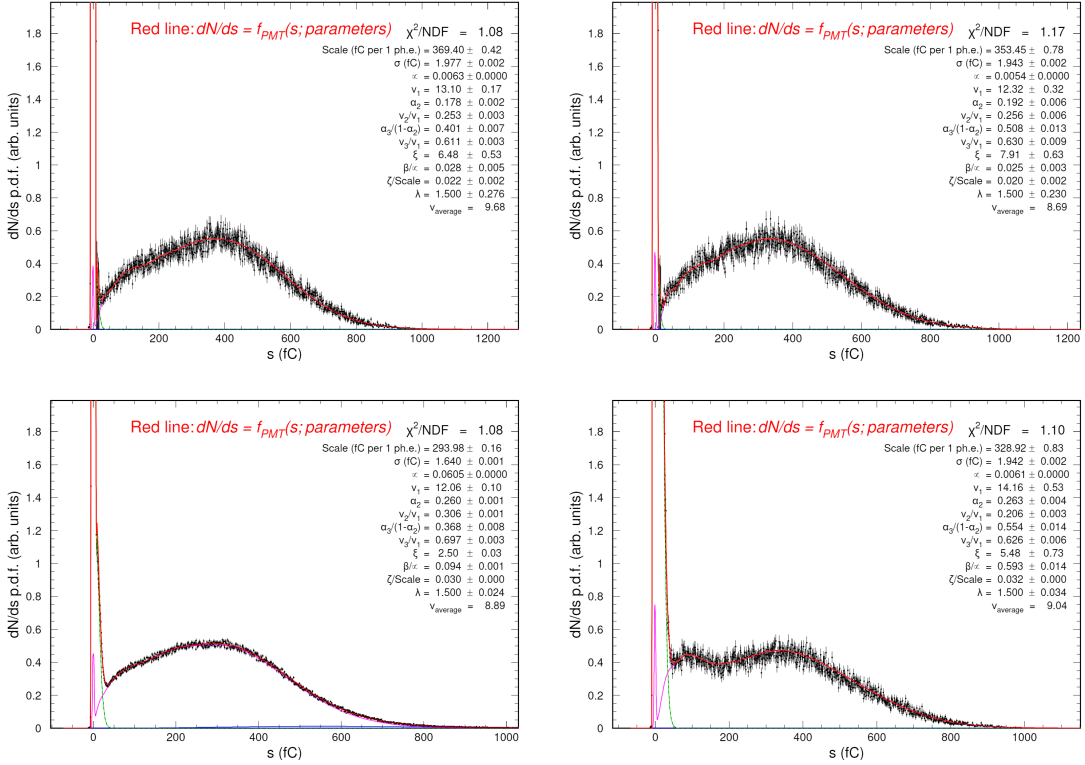


Figure 23: SPE probability distributions for PMT CA7811 (H8500), pixel 9, at HV = 1000 V. Top Left: 3mm mask. Bottom left: 6mm mask. Top right: run with full PMT face open, cross-talk events removed by the correlation analysis. Bottom right: run with full PMT face open, the contribution to the spectrum from the cross-talk events is approximated and parameterized by the analysis algorithm. The cross talk effects are too wide to be approximated correctly.

- [6] M. Contalbrigo, et al., The large-area hybrid-optics CLAS12 RICH detector: Tests of innovative components, Nucl. Instrum. Meth. A766 (2014) 22–27.
- [7] Hamamatsu multianode pmt h8500, (????). https://www.hamamatsu.com/resources/pdf/etd/H8500_H10966 TPMH1327E.pdf.
- [8] Hamamatsu multianode pmt h12700, (????). https://www.hamamatsu.com/resources/pdf/etd/H12700_H14220 TPMH1379E.pdf.
- [9] E. H. Bellamy, G. Bellettini, F. Gervelli, M. Incagli, D. Lucchesi, C. Pagliarone, F. Zetti, Yu. Budagov, I. Chirikov-Zorin, S. Tokar, Absolute calibration and monitoring of a spectrometric channel using a photomultiplier, Nucl. Instrum. Meth. A339 (1994) 468–476.
- [10] P. Degtiarenko, Precision analysis of the photomultiplier response to ultra low signals, Nuclear Instruments and Methods in Physics Research Section A: Accelerators, Spectrometers, Detectors and Associated Equipment 872 (2017) 1 – 15.

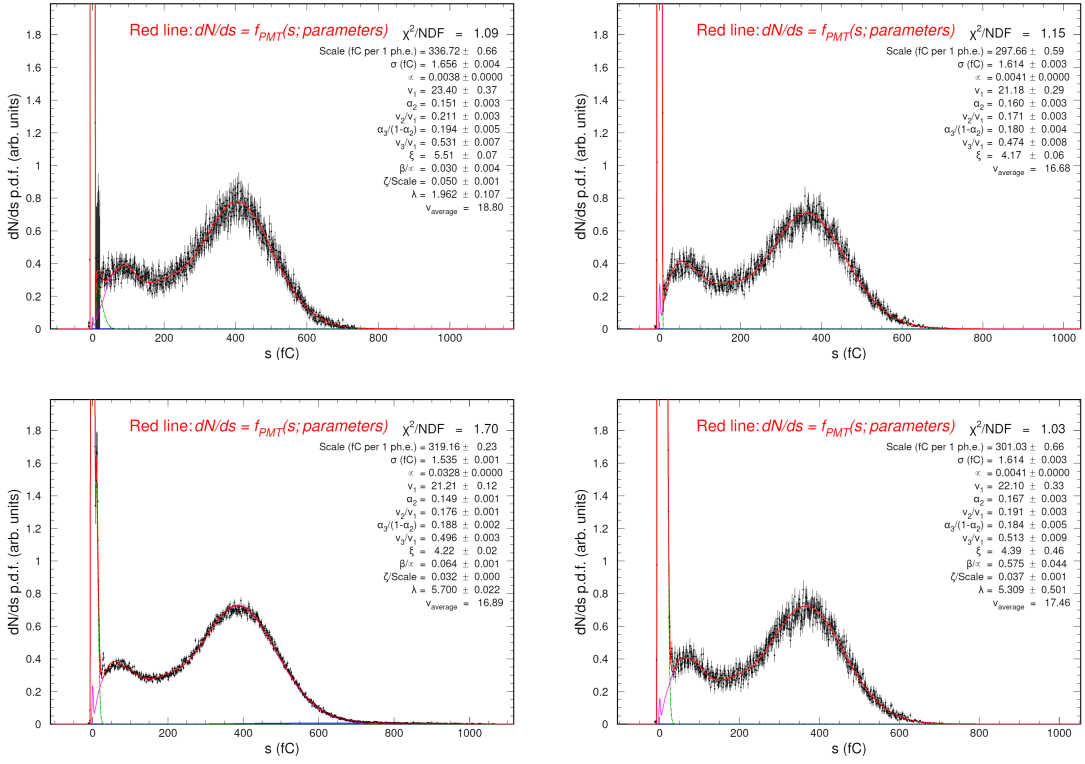


Figure 24: SPE probability distributions for PMT GA0516 (H12700), pixel 9, at HV = 1000 V. Top Left: 3mm mask. Bottom left: 6mm mask. Top right: run with full PMT face open, cross-talk events removed by the correlation analysis. Bottom right: run with full PMT face open, the contribution to the spectrum from the cross-talk events is approximated and parameterized by the analysis algorithm.

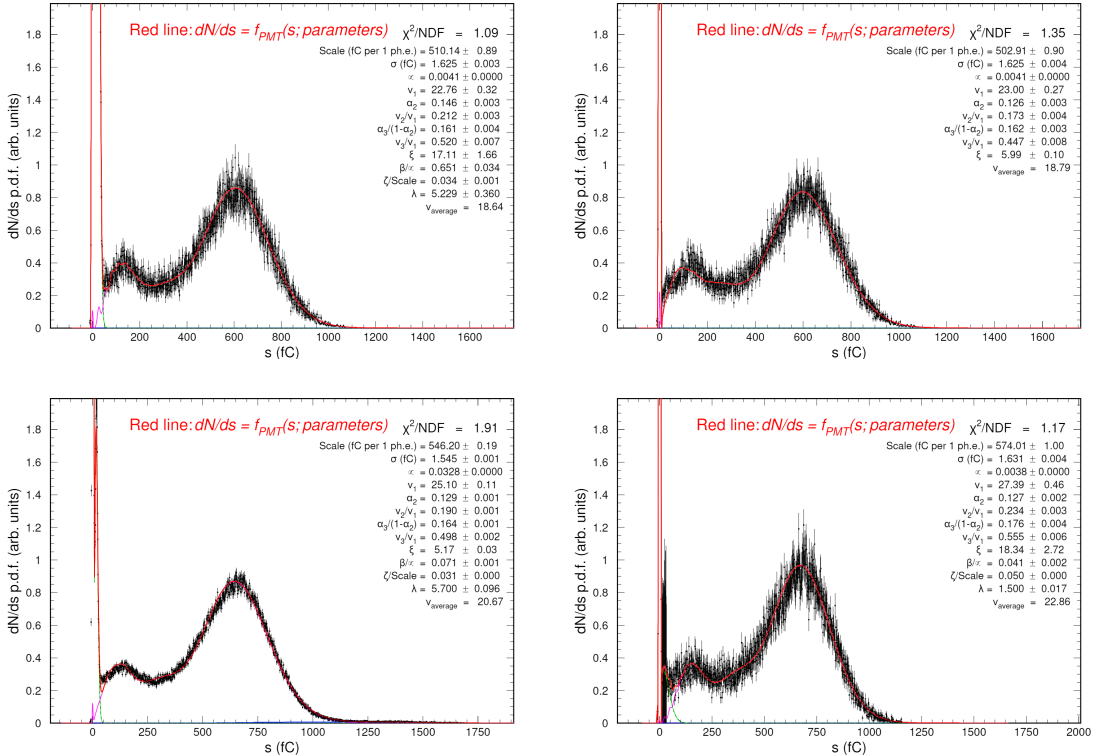


Figure 25: Same as Fig. 24, but all the data taken at HV = 1100 V.

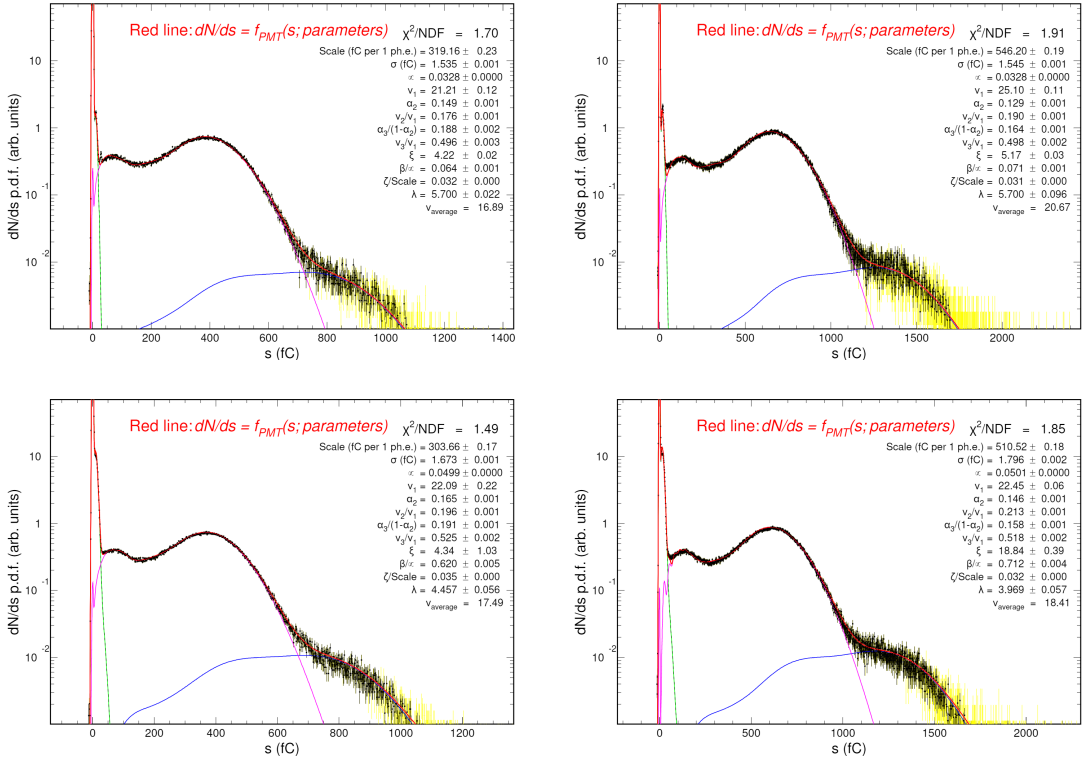


Figure 26: SPE probability distributions for PMT GA0516, pixel 4, wheel position 2, at HV = 1000 V (left plots) and at HV = 1100 V (right plots). Top plots: run with 6 mm mask covering the full PMT face except pixel 4. Bottom plots: run with full PMT face open, the contribution to the spectrum from the crosstalk events is approximated and parametrized by the analysis algorithm.

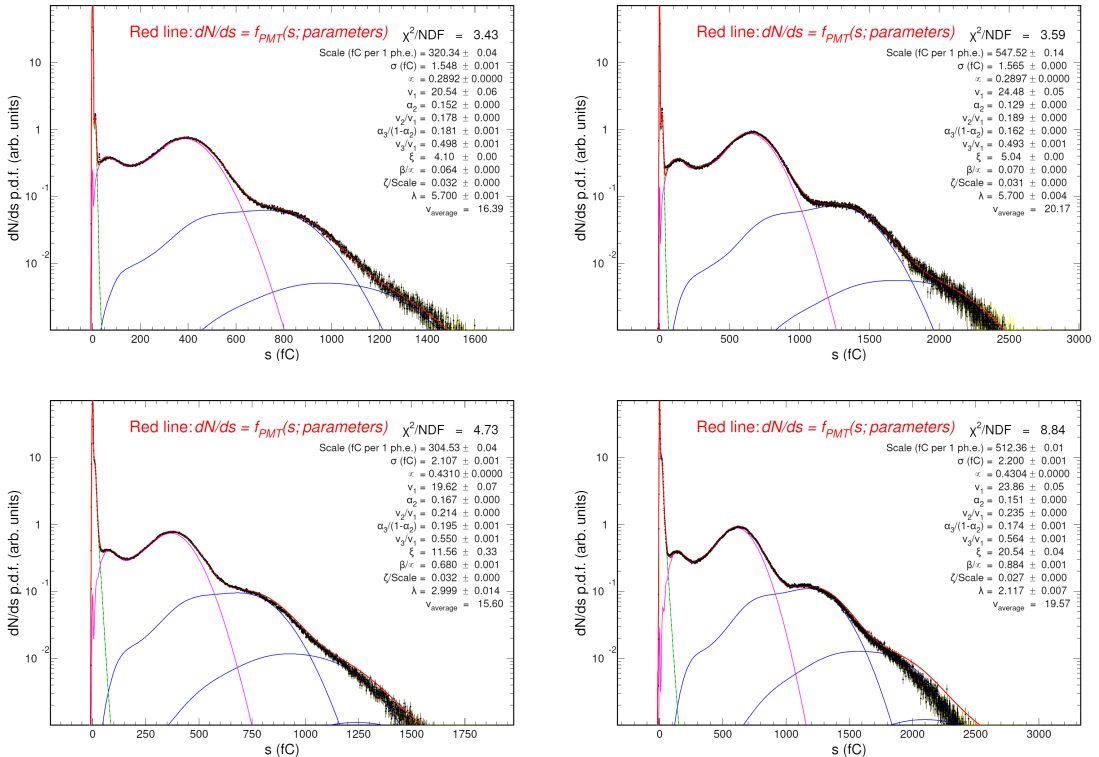


Figure 27: Same as Fig. 26 but at the wheel position 1.

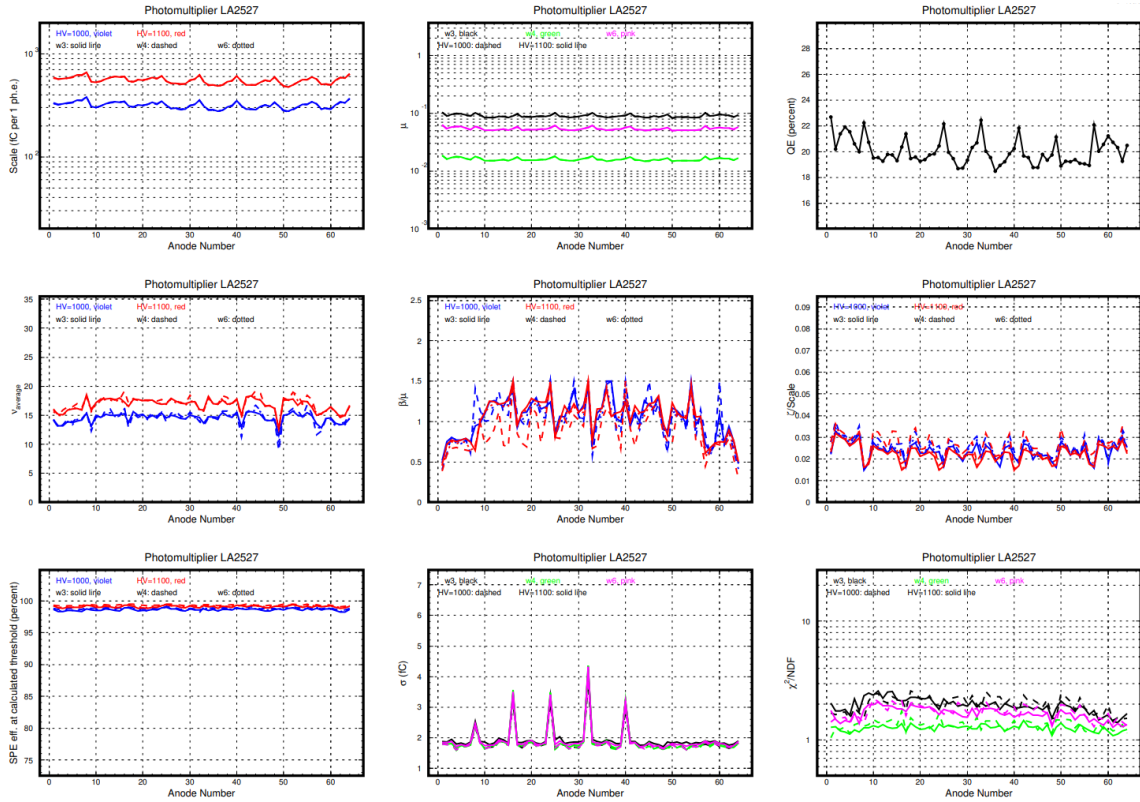


Figure 28: Illustration of the "PSPMT Passport" plots for one of the tubes, LA2527. The standard six measurements included runs at three illumination settings (wheel positions 3, 4, and 6), each at two operating high voltage values (1000 V. and 1100 V.).

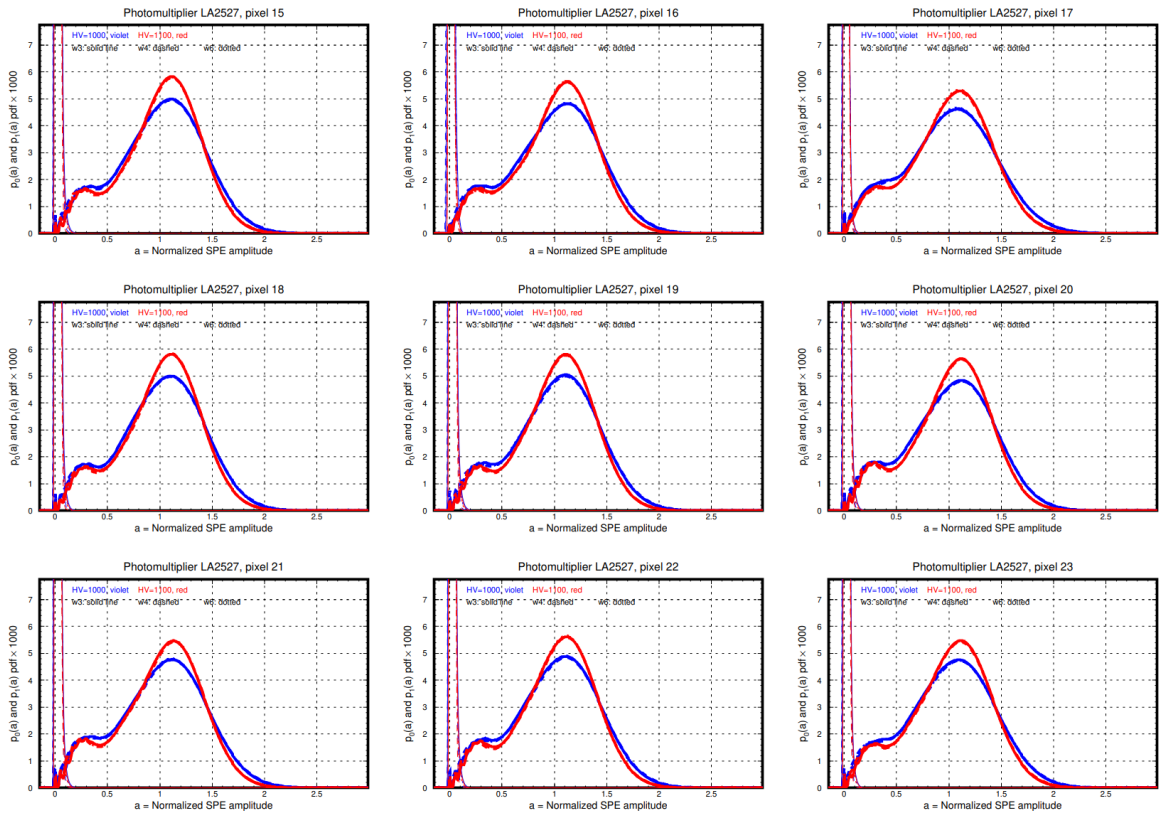


Figure 29: Illustration of the "PSPMT Passport" plots for one of the tubes, LA2527, continued. The standard six measurements included runs at three illumination settings (wheel positions 3, 4, and 6), each at two operating high voltages (1000 V, and 1100 V). Shown are the calculated SPE functions, defined by the fit parameters resulting from the independent fitting procedures for each six settings. Blue color corresponds to the three sets at $HV = 1000$ V, and red - to the runs at $HV = 1100$ V. The fit parameters of the independent fits at three different illuminations result in very stable SPE shapes, essentially overlapping each other in the plots.

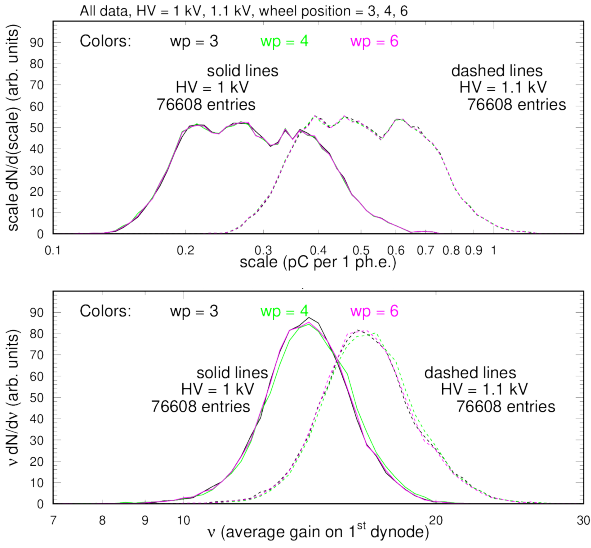


Figure 30: Distribution of scale (average charge per ph.e) and v (average gain on 1st dynode) as determined by the fitting procedure for a set of 399 PMTs.

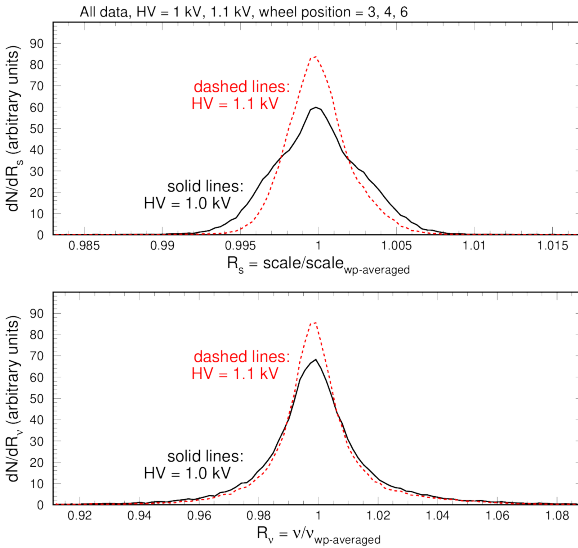


Figure 31: Scale and v averaged over three different illumination settings (wheel positions 3, 4, and 6).

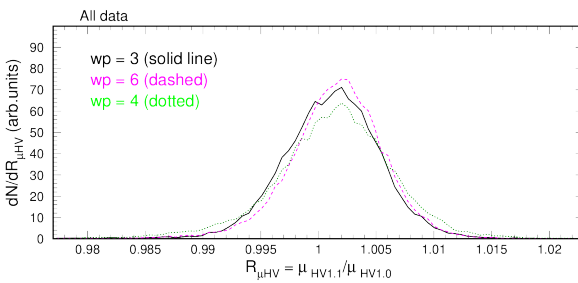


Figure 32: The ratio of the μ parameters from the fit results at HV = 1100 V to the results at HV = 1000 V.

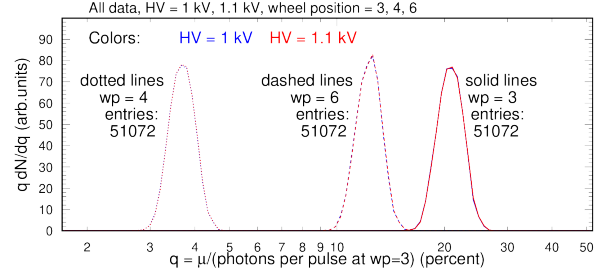


Figure 33: Distribution of μ divided by the measured number of photons per pulse at wheel position 3. For the data collected at wheel position 3, this ratio is the quantum efficiency of the individual pixels.

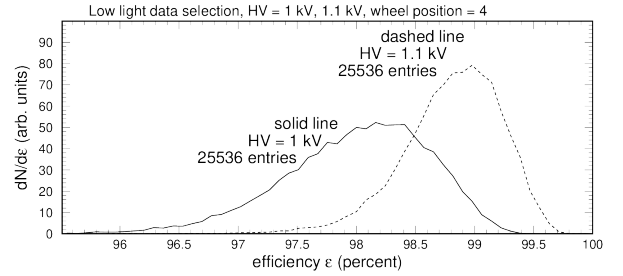


Figure 34: Distribution of the measured efficiency for all pixels at wheel position 4.

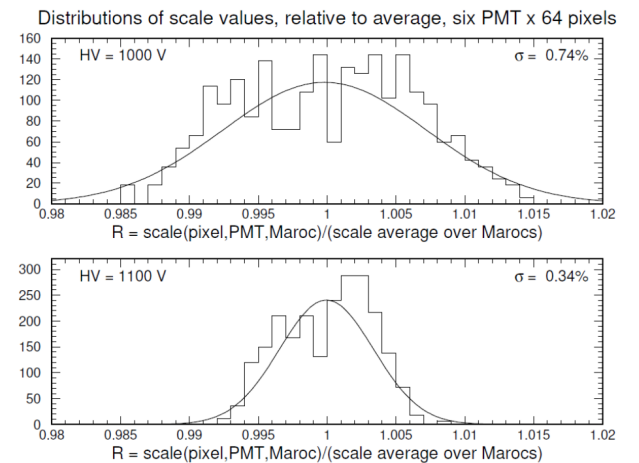


Figure 35: Evaluated precision of the scale parameter measurement for the two high voltage settings.

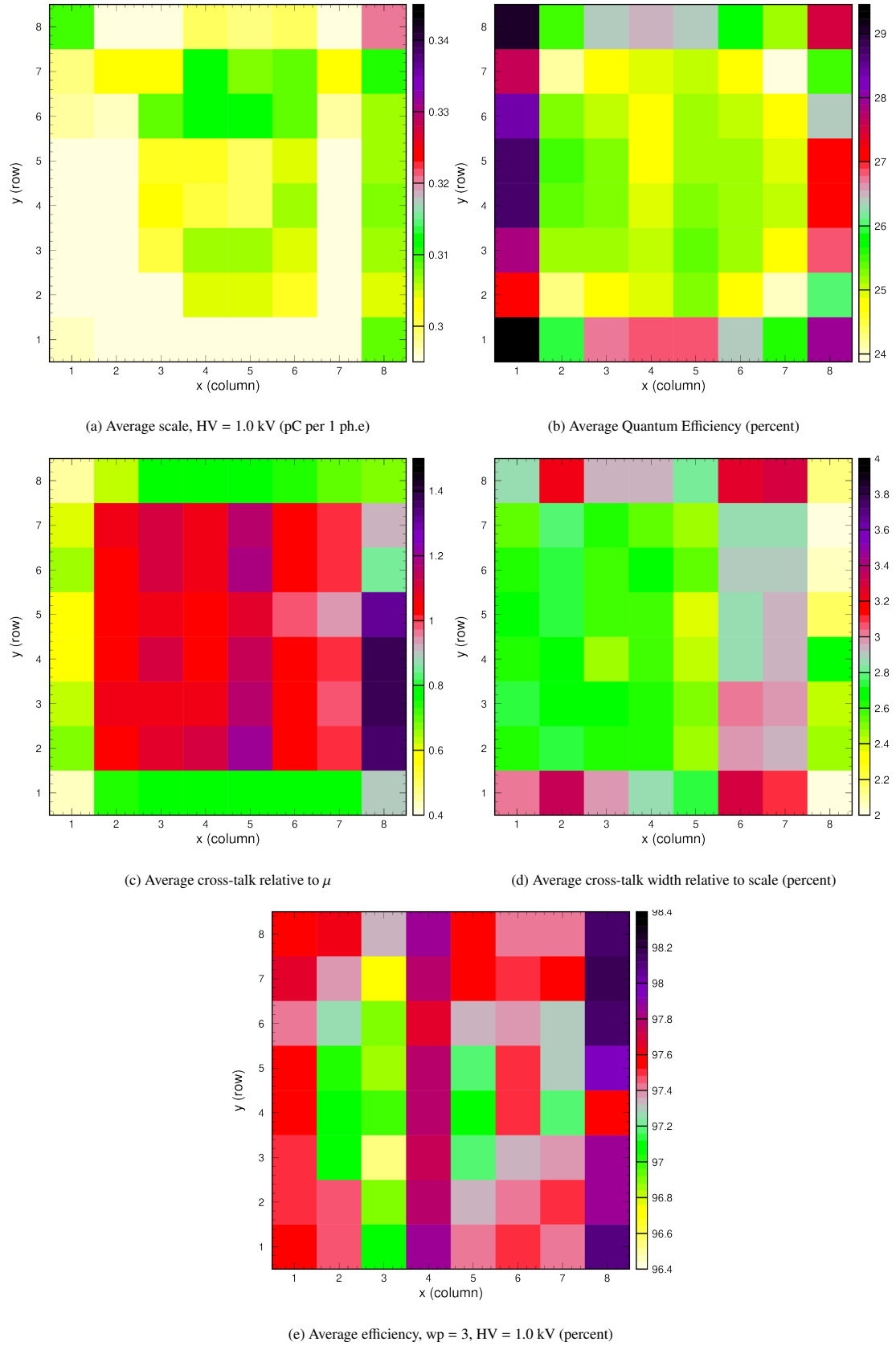


Figure 36: Two dimensional plots showing the average (a) scale, (b) quantum efficiency, (c) cross-talk relative to μ , (d) cross-talk relative to scale, and (e) efficiency as a function of pixel location.